

Numerical simulation of supersonic impinging jet flows using Reynolds averaged Navier–Stokes and Large Eddy Simulation

L. Chan¹, C. Chin¹, J. Soria^{2,3} and A. Ooi¹

¹Department of Mechanical Engineering
 University of Melbourne, Victoria 3010, Australia

²Laboratory for Turbulence Research in Aerospace & Combustion
 Department of Mechanical and Aerospace Engineering
 Monash University, Victoria 3800, Australia

³Department of Aeronautical Engineering
 King Abdulaziz University, Jeddah 21589, Kingdom of Saudi Arabia

Abstract

The flow structures of a supersonic impinging jet are investigated via numerical simulation. A converging inlet nozzle is used to accelerate the flow to sonic velocity and the flow impinges on a wall located at a normalized stand-off distance (z/D) of 2.5. The Reynolds averaged Navier–Stokes (RANS) and the Large Eddy Simulation (LES) methodologies are used to simulate the shock structures of the impinged jet. The characteristics of the underexpanded supersonic impinging jet is then visually analysed in the LES model. Next, the results of the numerical simulations are compared to experimental data obtained by [7], which uses Schlieren photography and shadowgraphy technique to visualize the shock structures. Results from the RANS and LES numerical models which are consistent with the experimental data demonstrate the capability of both methodologies in simulating supersonic impinging jet flows.

Introduction

Impinging jets have numerous practical applications and are used in the cold gas dynamic spraying process, short take-off and vertical landing (STOVL) aeroplanes and in the electronics industry. Due to its various applications in multiple industries, many aspects of the impinging jet have been researched. [14] researched the heat transfer capability of impinging jets using numerical methods and [3] conducted an experimental study on using impinging jets to cool turbine blades. Another aspect which is of interest is the noise and acoustic waves of supersonic impinging jets emitted by STOVL aeroplanes. [2] and [6] performed LES to obtain the amplitude and frequency of the acoustic waves.

This paper will analyse the potential of the RANS and LES models in simulating compressible flows. The LES model resolves the large eddies and models the small eddies in the flow. It is therefore able to accurately predict the large structures in the flow but is computationally expensive. On the other hand, the RANS model uses only a fraction of the LES model's computational resources and is able to provide adequate accuracy of the flow field for most engineering applications.

Previously, [8, 13, 11] have used the RANS model to simulate the cold spray process and results are consistent with the experimental data. As reported by [8], a numerical simulation of a supersonic impinging jet laden with particles was conducted and compared with experimental values. The Reynolds Stress Model (RSM), which is a second order RANS closure method is used in the simulation. This model takes into account the rotation and rapid changes in the strain rate more vigorously than the $k-\epsilon$ model and is more accurate in predicting the flow struc-

tures [9]. The particle distribution and impact velocity of the cold spray particles which are important factors in determining the quality of the coating, were consistent with the experimental findings.

Therefore, this paper aims to further investigate the accuracy of the selected RANS turbulence model in simulating the flow features of an underexpanded supersonic impinging jet and whether the additional computational cost required for the LES model is justifiable. In this paper, the RANS simulation will use the standard $k-\epsilon$ turbulence model. This turbulence model is one of the most widely used model as it is computationally cheap, robust and adequate in predicting flows. As for the LES simulation, the Smagorinsky subgrid scale (SGS) model will be used. This SGS model was first introduced by Smagorinsky in 1963 to simulate air currents in the atmosphere for weather forecasting purposes [10] but is now used to perform simulations for many different flow fields.

Numerical Models

Reynolds Averaged Navier–Stokes Model

The RANS model is based on the concept of Reynolds averaging, where a turbulence property, f can be decomposed into 2 parts, a mean, \bar{f} and fluctuating component, f' . To account for the effects of compressibility, Favre averaging, which is similar to Reynolds averaging with the exception that the mean term is density averaged, has to be used. The Favre averaged mean and fluctuating terms are denoted by \bar{f} and f'' . Applying the Reynolds averaging to the density and pressure terms and Favre averaging to the other terms in the Navier–Stokes equation will lead to the Favre and Reynolds averaged Navier–Stokes equation [12]. The equations have 9 unknowns—6 from the Favre averaged Reynolds stress, τ_{ij}^F and 3 from the turbulent heat flux, q_j^T . To close the equations, 2 equation $k-\epsilon$ turbulence model will be used. This turbulence model is based on Boussinesq eddy viscosity hypothesis, where τ_{ij}^F is related to the eddy viscosity, μ_T by equation (1)

$$\tau_{ij}^F = -\bar{\rho} \widetilde{u_i'' u_j''} = 2\mu_T \tilde{S}_{ij} - \frac{2\delta_{ij}}{3} \left(\mu_T \frac{\partial \bar{u}_k}{\partial x_k} - \bar{p} \bar{k} \right) \quad (1)$$

where \tilde{S}_{ij} is the strain tensor. In addition, the Reynolds analogy is used to model the turbulent heat flux vector, forming equation (2).

$$q_j^T = -\kappa_T \frac{\partial \bar{T}}{\partial x_j} \quad (2)$$

κ_T is the turbulent heat coefficient. Similar to eddy viscosity, the turbulent heat coefficient is not a physical property of the

flow but occurs as a result of turbulence. The $k - \varepsilon$ turbulence model uses the turbulent kinetic energy, k and the turbulent dissipation rate, ε transport equation (3, 4) to calculate the eddy viscosity.

$$\frac{\partial}{\partial t}(\rho k) + \frac{\partial}{\partial x_i}(\rho u_i k) = \frac{\partial}{\partial x_j} \left[\left(\mu + \frac{\mu_T}{\sigma_k} \right) \frac{\partial k}{\partial x_j} \right] + G_k - \frac{2}{3} \frac{\partial u_i}{\partial x_j} \rho k \delta_{ij} - \rho \varepsilon \quad (3)$$

$$\frac{\partial}{\partial t}(\rho \varepsilon) + \frac{\partial}{\partial x_i}(\rho u_i \varepsilon) = \frac{\partial}{\partial x_j} \left[\left(\mu + \frac{\mu_T}{\sigma_\varepsilon} \right) \frac{\partial \varepsilon}{\partial x_j} \right] + C_1 G_k \frac{\varepsilon}{k} - \left(\frac{2}{3} C_1 + C_3 \right) \frac{\partial u_i}{\partial x_j} \rho \varepsilon \delta_{ij} - C_2 \rho \frac{\varepsilon^2}{k} \quad (4)$$

where the production of turbulent kinetic energy due to the mean velocity gradients, G_k is as in equation (5).

$$G_k = \mu_T \left(\frac{\partial u_i}{\partial x_j} + \frac{\partial u_j}{\partial x_i} \right) \frac{\partial u_i}{\partial x_j} \quad (5)$$

and $\rho \varepsilon$ is the turbulent energy dissipation rate. The turbulent viscosity, μ_T and the turbulent heat coefficient, κ_T are then calculated using equation (6).

$$\mu_T = \rho C_\mu \frac{k^2}{\varepsilon}, \quad \kappa_T = c_p \frac{\mu_T}{Pr_T} \quad (6)$$

The coefficients used in the simulation are: $Pr_T = 1$, $C_1 = 1.44$, $C_2 = 1.92$, $C_3 = -0.33$, $C_\mu = 0.09$, $\sigma_k = 1.0$, $\sigma_\varepsilon = 1.3$.

Large Eddy Simulation Model

The LES model uses a spatial filtering method where a turbulence property can be decomposed into a filtered and a sub-filtered part. The filtered component is resolved numerically while the sub-filtered part is modelled. In this paper, a box filter function with a filter width equivalent to the cube root of cell volume is used. To account for the compressibility of the fluid, Favre filtering is applied to the Navier–Stokes equation resulting in the Favre filtered Navier–Stokes equation as stated by [1]. To close the equations, the SGS stress tensor, B and the SGS flux vector, b has to be modelled. The Smagorinsky SGS model, which is used in the simulation relies on the eddy viscosity and diffusivity hypothesis based on local equilibrium [4]. Therefore, the SGS stress tensor and SGS flux vector is defined as in equation (7) and (8). This model is an algebraic model and does not need any additional transport equations.

$$B = 2\mu_{SGS} \tilde{S}_{ij} - \frac{2\tilde{\delta}_{ij}}{3} \left(\mu_{SGS} \frac{\partial \tilde{u}_k}{\partial x_k} - \tilde{\rho} \tilde{k} \right) \quad (7)$$

$$b = -\kappa_{SGS} \frac{\partial \tilde{T}}{\partial x_j} \quad (8)$$

The eddy viscosity, μ_{SGS} and the turbulent heat coefficient, κ_{SGS} are defined in equation (9).

$$\mu_{SGS} = C_k \rho \Delta k^{1/2}, \quad \kappa_{SGS} = \frac{\mu_{SGS}}{Pr_T} \quad (9)$$

The SGS kinetic energy, k can be calculated by solving equation (10)

$$-\frac{C_e \rho k^{3/2}}{\Delta} = \frac{2}{3} \rho k \tilde{S}_{kk} \delta_{ij} - 2C_k \Delta k^{1/2} (\tilde{S}_{ij})^2 \quad (10)$$

The value of the constants are: $C_e = 1.048$ and $C_k = 0.07$.

Computational Setup

A compressible transient solver using the finite volume method is applied to solve the governing equations. The time derivative is discretised using the second order backward Euler method to ensure stability. As for the pressure and velocity divergence term, the second order central differencing discretisation method is used as it reduces the numerical error in the LES simulation. The computational parameters for both the RANS and LES model are as in table 1. $\Delta r/D$, $\Delta r\theta/D$ and $\Delta z/D$ are the normalized grid size in the radial, azimuthal and axial direction and N_p denotes the total number of points in the LES and RANS mesh. The ratio between the stagnation quantity at the nozzle inlet to the ambient are identified by the o and ∞ .

$\Delta r/D$	$\Delta r\theta/D$	$\Delta z/D$
[4E-5, 0.467]	[7.838E-3, 0.75]	[0.0217, 0.145]
N_p	P_o/P_∞	T_o/T_∞
3,808,586	3.5	1

Table 1: Computational parameters.

The converging nozzle which was used by [7] follows the curve of a third order polynomial as in equation (11).

$$r = a.z^3 + b.z^2 + c.z + d \quad (11)$$

where $a = -0.00028$, $b = 0.021$, $c = 0$, $d = 2.5$. The inlet of the nozzle has a diameter of $8D$ and $D = 5\text{mm}$ is the diameter of the exit nozzle. The impinging plane is located at a normalised stand-off distance (z/D) of 2.5 from the nozzle exit as illustrated in figure 1. To ensure that the viscous sublayer of the flow is resolved, the first grid point from the nozzle wall is located at a distance of $y^+ < 1$. On the other hand, mesh located away from the impinging area is graded gradually coarser as in figure 2. The walls of the converging nozzle and the impinging plane are adiabatic and follow the no-slip condition.

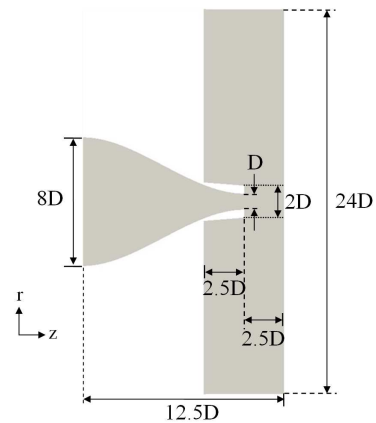


Figure 1: Mesh geometry

Results

The various characteristics of an underexpanded supersonic impinging jet simulated LES are illustrated in figure 3. As the LES model is inherently three-dimensional and unsteady, the propagation of the impinging tones and the transient behaviour of the jet's shear layer, oblique and bow shock can be observed in figure 4. These pictures are time normalised by the flow cycle period, ($T_{norm} = T/t_{cyc}$) which is the average time taken for

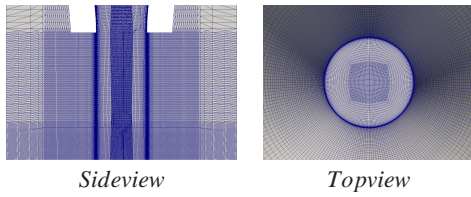


Figure 2: Side and top view of the mesh grid.

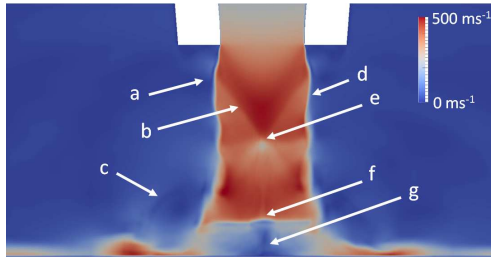


Figure 3: Instantaneous centreline slice velocity profile of LES. (a) Mach wave radiation, (b) Oblique shock, (c) Impingement tones, (d) Jet shear layer, (e) Mach disk, (f) Bow shock, (g) Recirculation zone.

the flow to propagate from the nozzle exit to the impingement plane. The flow cycle period is calculated by dividing the stand-off distance with the nozzle exit velocity ($t_{cyc} = 2.5D/U_{exit}$). The Q criterion isosurfaces are plotted and the values are chosen

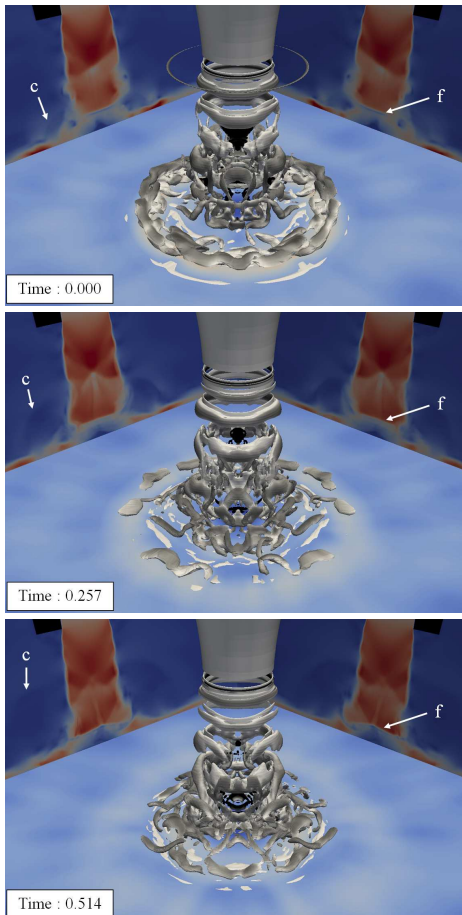


Figure 4: Instantaneous visualisation of Q isosurfaces and velocity field of LES at three different normalised time. (c) Impingement tones, (f) Bow shock

to better visualize the flow properties. The Q criterion, defined by the second invariant of the velocity tensor, is a method proposed by Hunt, Wray and Moin (1988) to characterise a vortex [5]. As the flow propagates from the nozzle exit, the formation of vortex rings are observed. These vortices then disperses into small, randomly orientated hair pin structures as they approach the vicinity of the impingement plane. To distinguish the rotational intensities of these structures, the isosurfaces are color-graded from black to white with black signifying regions of low vorticity and white, the converse. Two slices of the velocity profile at the centreline perpendicular to each other and a slice located at normalised distance of $z_{imp}/D = 0.01$ from the impingement plane are plotted to observe the propagation of the impingement tones. The pulsating instability of the bow shock is observed in the velocity field as its shape changes from a flat surface ($T_{norm} = 0.000, 0.257$) to a curved surface ($T_{norm} = 0.514$). Moreover, the intensity and also the diameter of the bow shock fluctuates with time. At $T_{norm} = 0.000$, propagating impingement tones form a vortex ring at the edge of the nozzle's outer wall boundary.

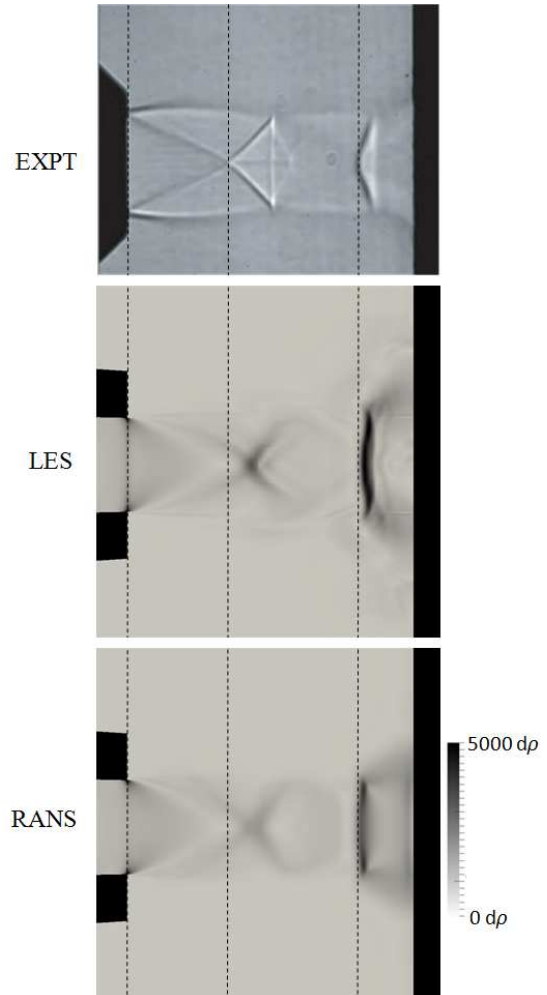


Figure 5: Shadowgraph and time averaged density gradient images of the supersonic impinging jet. From top: Experiment [7], LES and RANS.

The visual comparison between the experiment [7], LES and RANS models are illustrated in figure 5. Results of the LES model is time averaged for a period of three flow cycles. The contours of the RANS and LES are standardised and adjusted to clearly visualise the shock structures. It can be observed that

the Mach disk length of the LES and RANS model are larger than the experimental value. However, the location of the bow shock near the impingement region is the same as in the experiment. In addition, it can also be seen that the intensity of

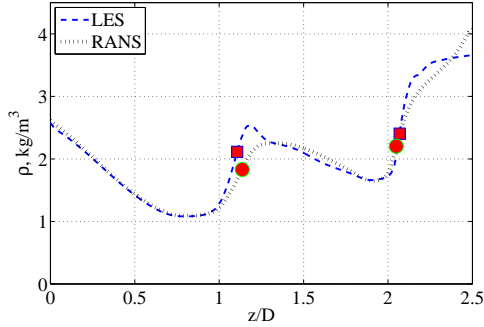


Figure 6: Centreline streamwise density profile of the RANS and LES simulation. Markers denote the location of the Mach disk and bow shock

the shock structures in the RANS simulation is faint and not as distinct as the one produced by the LES simulation. This is consistent with the plot of the centreline streamwise density in figure 6 which shows that the shock in the LES is located at a higher density slope. The location of the Mach disk is obtained by calculating the local maximum density gradient. The values of the normalized Mach disk length, ($Z_M = z_M/D$) and the errors of the simulation relative to the experimental data are tabulated in table 2. The overly dissipative nature of the $k - \epsilon$ RANS turbulence model which will cause overspreading of the jet is not observed in both the streamwise and spanwise direction and is consistent with the LES model as seen in figure 6 and 7. The characteristic of this model is not observed due to the short impinging distance.

	Experiment	RANS	LES
Z_M	1.001	1.137	1.107
% Error	-	13.59	10.59

Table 2: Normalised Mach disk length, Z_M for Experiment [7], RANS and LES

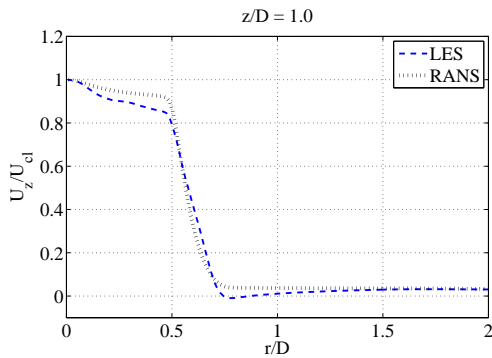


Figure 7: Normalised radial velocity profile of the RANS and LES simulation at $z/D = 1$.

Conclusion

The LES and RANS model for an underexpanded supersonic impinging jet is analysed and compared with experimental data. Both the LES and RANS models produced results which are

consistent with the results obtained by [7]. The dissipative characteristic of the RANS model is not observed due to the short stand-off distance. In addition, the flow characteristics of the LES model is also discussed in detail and the unsteadiness of the underexpanded supersonic impinging jet is visually inspected. Overall, both the RANS and LES models are suitable in predicting the flow of an underexpanded supersonic jet, with the LES model being slightly more accurate.

Acknowledgements

The authors would like to acknowledge the financial support of the Australian Research Council.

References

- [1] Blazek, J., *Computational Fluid Dynamics: Principles and Applications*, Elsevier, 2005.
- [2] Erwin, J. P. and Sinha, N., Large eddy simulation of supersonic impinging jets, in *AIAA Aerospace Sciences Meeting*, 2012.
- [3] Esposito, E. I., Jet impingement cooling configurations for gas turbine combustion, 2006.
- [4] Fureby, C., On subgrid scale modeling in large eddy simulations of compressible fluid flow, *Phys. Fluids*, **8**, 1996, 1301–1311.
- [5] Hunt, J. C. R., Wray, A. and Moin, P., Eddies, stream, and convergence zones in turbulent flows, in *Center for Turbulence Research Report*, CTR-S88, 1988.
- [6] Nelson, C. C. and Cain, A. B., Simulations of high speed impinging jets, in *AIAA Aerospace Sciences Meeting*, 2012.
- [7] Risborg, A., High speed optical investigation of shock-wave instabilities in an underexpanded impinging jet, 2008.
- [8] Samareh, B., Stier, O., Luthen, V. and Dolatabadi, A., Assessment of cfd modeling via flow visualization in cold spray process, *J. Therm. Spray Technol.*, **18**, 2009, 934–943.
- [9] Sarkar, S., Erlebacher, G., Hussaini, M. and Kreiss, H., Analysis and modeling of dilatation term in compressible turbulence, *J. Fluid Mech.*, **227**, 1991, 473–493.
- [10] Smagorinski, J., General circulation experiments with the primitive equations, *Mon. Weather Rev.*, **91**, 1963, 99.
- [11] Tien-Chien, J., Longjian, L., Wenzhi, C., Qinghua, C. and Xinming, Z., Numerical investigation on cold gas dynamic spray process with nano- and microsize particles, *Int. J. Heat and Mass Transfer*, **48**, 2005, 4384–4396.
- [12] Wilcox, D. C., *Turbulence modelling for CFD*, DCW Industries, 1994.
- [13] Yin, S., Xiao-Fang, W., Wen-Ya, L. and Bao-Peng, X., Numerical study on the effect of substrate angle on particle impact velocity and normal velocity component in cold gas dynamic spraying based on CFD, *J. Therm. Spray Technol.*, **19**, 2010, 1155–1162.
- [14] Zuckerman, N. and Lior, N., Jet impingement heat transfer: Physics, correlations, and numerical modeling, *Adv. Heat Transfer*, **39**, 2006, 565–631.